Pushing Wireless Charging from Station to Travel

Lili Chen[1], Bozhong Yu[2], Yongjian Fu[3], Ju Ren[1,4*], Hao Pan[5], Jeremy Gummeson[6],
Yaoxue Zhang[1,4]
[1]Department of Computer Science and Technology, BNRist, Tsinghua University
[2]School of Information Science and Technology, Northwest University
[3]School of Computer Science and Engineering, Central South University
[4]Zhongguancun Laboratory, Beijing, China, [5]Microsoft Research Asia
[6]Department of Electrical and Computer Engineering, University of Massachusetts Amherst
{lilichen,renju,zhangyx}@tsinghua.edu.cn,yubozhong@stumail.nwu.edu.cn,fuyongjian@csu.edu.cn
panhao@microsoft.com,jgummeso@umass.edu

ABSTRACT

Wireless charging has achieved promising progress in recent years. However, the severe bottlenecks are the small charging range and poor flexibility. This paper presents ChargeX to enable smart and long-range wireless charging for small mobile devices. ChargeX incorporates emerging smart metasurface into the magnetic resonance coupling-based wireless charging to extend the charging range and accommodates the mobility of charging device. Unlike previous endeavors in metasurface-assisted wireless charging that focused on simulation, ChargeX makes efforts across software and hardware to meet three crucial requirements for a practical wireless charging system: (i) realize high-freedom and accurate metasurface control under the premise of low loss; (ii) obtain real-time feedback from the receiver and make effective manipulation for transmitted magnetic flux; and (iii) generate a proper AC signal source at the desired frequency band. We developed a prototype of ChargeX, and evaluated its performance through controlled experiments and real-world phone charging. Extensive experiments demonstrate the great potential of ChargeX for long-range and flexible wireless charging with a compact receiver design.

KEYWORDS

Wireless charging, magnetic-beamforming, metasurface

ACM Reference Format:
Lili Chen[1], Bozhong Yu[2], Yongjian Fu[3], Ju Ren[1,4*], Hao Pan[5], Jeremy Gummeson[6], Yaoxue Zhang[1,4]. 2024. Pushing Wireless Charging from Station to Travel. In *Proceedings of The 30th Annual International Conference On Mobile Computing And Networking (ACM MobiCom'24).* ACM, New York, NY, USA, 16 pages. https://doi.org/10.1145/3636534.3649346

1 INTRODUCTION

Wireless power transfer (WPT) was first introduced over 100 years ago, and has seen a surge in applications since the fourth industrial revolution. WPT is now gaining popularity in the smart mobile internet of things (IoT) industry as it promises increased mobility and freedom while charging devices [4, 20]. However, despite the availability of wireless chargers for many mobile devices, they are not nearly as cool as they sound. We are still constrained by the need to place our devices on a charging pad, which may result in slow charging or a lack of charging altogether if the device's charging coil is not aligned properly with the charger. This is not the kind of wireless charging that many of us expected. We desire the ultimate freedom to charge our mobile phones or portable devices without worrying about forgetting to charge or experiencing inconvenience during charging.

In this paper, we attempt to bring wireless charging to the next stage of truly wireless, pushing it from *station* to *travel*. We demonstrate that it is possible to achieve WPT technology with **(a) guaranteed safety** - ensuring that electromagnetic waves do not pose a threat to humans or other biological life, **(b) long range** - allowing devices to be charged from meter level away from the charger, and **(c) high tunability** - enabling devices to be placed or moved freely during charging. Our goal is to wirelessly charge small mobile devices without impeding their inherent mobility and normal operation. Such a WPT system holds great promise in reality, especially for individuals who are constantly on the go, browsing the web, or playing games, etc. While our focus is on benefiting small mobile devices, we hope that this work will inspire the

---

[*] Corresponding author.

ACM MobiCom'24, November 18–22, 2024, Washington, D.C., USA

ACM ISBN 979-8-4007-0489-5/24/09
https://doi.org/10.1145/3636534.3649346

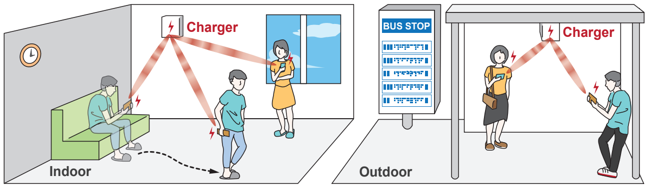

Figure 1: Motivation examples of ChargeX.

design of wireless charging systems for electric vehicles that can charge while driving.

We acknowledge the numerous endeavors aimed at advancing WPT technology. The traditional approach for WPT involves inductive coupling, which can exhibit high efficiency when the transmitter and receiver coils are meticulously aligned within a few centimeters of each other. A significant breakthrough in WPT occurred with the introduction of magnetic resonance coupling [17]. This technology enables the transmitter and receiver circuits to resonate at the same frequency, facilitating robust mid-range WPT up to around 20 cm [3, 14]. Magnetic resonance coupling-based WPT (MR-WPT) is considered safe as magnetic fields have weak interactions with living organisms [31]. Furthermore, MagMIMO utilizes a multiple-transmitter-based beamforming technique to direct magnetic flux towards the receiver, extending power transfer distances to about 40 cm [14]. However, the aforementioned near-field coupling methods still have limitations related to distance and mobility. On the contrary, far-field radiation-based WPT systems (such as microwave and laser) have been proposed to achieve lengthy transfer distances of several meters [11, 22, 29]. Yet, these radiative approaches require a clear line of sight and can be obstructed by intervening objects, potentially posing risks to living organisms depending on the transmission power level [15]. Thus, previous endeavors have not fully met all the criteria we have envisioned.

This paper presents ChargeX, a system that enables smart, safe, and long-range wireless charging without requiring devices to be in close proximity to the charging pad. ChargeX employs magnetic resonance coupling between the transmitter (Tx) and receiver (Rx) to ensure the safe and efficient wireless charging over a moderate range. To further extend the charging distance and accommodate the movement of device, we propose involving a tunable metasurface (MTS) to focus the magnetic field towards the Rx in real-time. The high-level idea seems intuitive, but it is difficult to implement it into a functional system.

Previous studies demonstrated that MTS brings significant efficiency gains to symmetric WPT systems [32, 37]. However, the existing work lacks the needed flexibility and continuous tunability in systems with a high Tx/Rx radius ratio, due to the absence of precise and high-freedom control of compensation capacitors on the MTS units [19, 26]. To fit the Rx coil into small mobile devices, it must be compact. However, the Tx coil can be larger (like a wall-hung mural), for higher efficiency benchmark. Therefore, to maximize the tunability of the MTS and achieve maximum WPT efficiency despite uneven sizes of the transceiver, it is imperative to achieve accurate and wide-range control of the MTS, which however is challenging in practice. On one hand, although the commercial programmable power supplies [10] can continuously control varactor diodes, their bulky size and limited channels (only 1 to 3) make them unsuitable for controlling MTS with many unit cells. Instead, we design a DAC-based [7], channel-scalable and programmable power supply to realize continuous and independent control of each unit on the MTS. On the other hand, varactor diodes with a wide capacitance range always suffer from non-negligible capacitance error, which affects the accuracy of MTS control. To solve this, we propose a software-based calibration mechanism to offset the inherent diode error.

After ensuring precise and high-freedom control of the MTS, the next step is to integrate it into an end-to-end transceiver system to achieve real-time magnetic beamforming, considering the frequent mobility of mobile devices during charging. For the purpose, the key is to obtain feedback from the Rx so that the optimal MTS configuration can be determined to induce the highest PTE from Tx to Rx. To do so, past MIMO based WPT system infers the voltage of Rx by measuring the real-time current of Tx based on the coupling effect between the Tx and Rx [14], which works well in static scenarios but is sensitive to surrounding interference, especially when the receiver is moving. This issue persists even if we adopt out-of-band communication. To enable robust wireless charging of mobile devices, this work introduces the combination of the coupling effect and out-of-band communication to deal with the interference issue. We determine the optimal MTS configuration based on the voltage and current values measured at both the Tx and Rx. Although we can achieve wireless communication between the Tx and Rx, and eventually the wire/wireless communication between the Tx and MTS controller, one may also be concerned about the deployment of MTS. Due to the mobility of devices and the coverage of MTS, it is unrealistic to place/move an MTS between the Tx and Rx in an open space. Fortunately, we observed that a closer distance between the MTS and Tx/Rx exhibits a higher PTE, which allows us to integrate the MTS at the Tx end for flexible deployment in reality.

Another practical issue we want to highlight is the frequency matching between the transceiver coils and source circuit. It is worth noting that most of wireless charging systems work at lower frequency bands, typically tens or hundreds of KHz, a extremely small Rx coil (i.e., $4-5$ cm diameter) cannot achieve magnetic resonance at such low frequency bands. To ensure the high efficiency and compact size, we choose 13.56 MHz as the resonant frequency of the Tx and Rx coils. However, the exiting 13.56 MHz source circuit is designed with very low input power (i.e., 1 W) since they target at the low power wearables. In this work, we tailored the source circuit to support a commonly desired power[1] (i.e., over 20 W) for popular mobile phones at the higher 13.56 MHz frequency band. The source circuit is also designed with adjustability to deal with the frequency shift of transceiver coils.

We built the prototype of ChargeX and evaluated it with various smartphones. The experimental results demonstrate that ChargeX outperforms both commercial wireless chargers and state-of-art wireless charging prototype. It charges unmodified devices with charging distances over 1 m and 60 cm when the input power is 50 W and 20 W, respectively, regardless of the use status and orientation of the devices.

Contributions. (i) To the best of our knowledge, ChargeX represents a pioneering practical effort to enable safe, long-range and flexible remote charging for small mobile devices by exploiting MTS-assisted magnetic beamforming, thereby pushing wireless charging from *station* to *travel*. (ii) For the purpose of compactness and long distance, we introduce a series of novel hardware designs including: transceiver coils, source/load circuits, and MTS controller. (iii) We propose a new wireless feedback mechanism to eliminate the interference issue in complex or mobile scenarios, ensuring a comprehensive end-to-end wireless charging system.

2 BACKGROUND AND OVERVIEW

2.1 Motivation and problem scope

As depicted in the conceptual illustration in Figure 1, ChargeX could be used in both indoor and outdoor scenarios. For instance, when users are using their phone during walking or at outside without bringing a charging pad. In these scenarios, flexible and long-range wireless charging is of high importance if a charger is deployed in surrounding infrastructure, but achieving such a vision is challenging because (a) technologies that support long-distance wireless charging is based on electromagnetic radiation that may cause harm to living organisms, and (b) safe technologies based on magnetic coupling is limited in charging distance and flexibility. ChargeX is designed to enable efficient wireless charging in such difficult settings, and push wireless charging to the next stage of truly wireless.

In this work, we aim to achieve the following two goals. The first is to beamsteer the magnetic flux from charger to make it direct to the small devices that require charging. The second is to manipulate the magnetic beam direction in real time to make it adaptable to device movement. For magnetic-beamforming purpose, we opt to incorporate a MTS between the Tx and Rx coils, rather than using multiple Tx coils. This choice is motivated by the fact that when the dimensions of the transmissive MTS and each individual Tx coil approximate the total size of the Tx coil array, the MTS can attain higher gain thanks to its unique subwavelength structural characteristics. Therefore, we employ the transmissive MTS in our practical charging system and propose an optimal deployment strategy. We believe that further exploration is warranted to leverage the advantages of both transmissive and reflective MTSs in various scenarios.

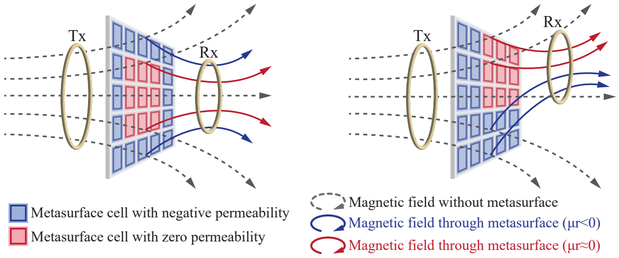

Figure 2: The magnetic field distribution of a WPT system with/without an MTS between the Tx and Rx.

2.2 Principle of MTS-assisted WPT

MTS-assisted WPT is a method for enhancing the efficiency of wireless power transfer by using an MTS, a two-dimensional array of subwavelength resonant structures, to manipulate the magnetic flux between the Tx and Rx coils [41]. The MTS can be placed between the Tx and Rx coils, and the resonant structures are designed to have specific electromagnetic properties that can be tuned by adjusting the geometry and composition of the individual units. When an alternating current (AC) is applied to the Tx coil, it generates a magnetic field that induces a current in the Rx coil. However, the efficiency of this process is limited by factors like the distance between the coils and the alignment of the coils relative to each other. By involving an MTS, the magnetic field can be manipulated to increase the amount of power transferred.

In particular, the MTS units can be designed to have a zero or negative permeability, which affects the propagation of the magnetic field. When the MTS units have a zero permeability, the magnetic field is not affected. However, when the MTS units have a negative permeability, the magnetic field is redirected and focused towards the Rx coil, which significantly increase the power transfer efficiency. As shown in Figure 2, a tunable MTS composed of units with different permeability can effectively change the direction of the magnetic flux depending on the location of Rx coil, since the

---

[1] The input power of most commercial wireless chargers ranges from 20W to 70W.

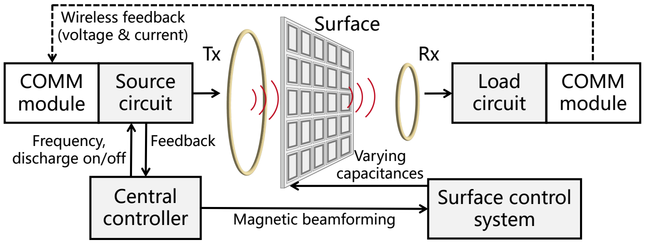

Figure 3: ChargeX system architecture.

negative refraction index of each unit cell can be tuned, thus compensating the low PTE resulting from the misalignments.

2.3 Overview

ChargeX is designed to remotely charge mobile devices, no matter if the user is moving or stationary. We aim for satisfying charging distance up to meter level, adapting to various device orientations, and even charging multiple devices simultaneously. The Rx is designed to be as small as a few centimeters, for easy integration into small mobile devices. The only assumption we have is that there is an inexpensive tunable MTS between the Tx and Rx. Considering the charging efficiency and practical deployment, we prefer to integrate the MTS to Tx end. As depicted in Figure 3, ChargeX consists of four innovative components:

An *MTS-assisted magnetic-beamsteering* mechanism to answer how a tunable MTS achieve the redirection of magnetic field, and how to manipulate the magnetic conductivity of MTS units to maximize energy transfer (see Section 3.1).

A *compact, efficient transceiver system* to provide potential for efficient wireless charging of portable mobile devices. For the purpose, the receiver should be designed small enough to be integrated into the device (see Section 3.2).

A *tunable MTS system* to redirect the magnetic field towards the receiver. To cope with the random position and movement of the receiving devices, the MTS should be programmed fully and quickly to achieve desired magnetic-beamsteering (see Section 3.3).

A *central controller* to control the switch of transmitter and beam-steering configuration of MTS in real time, according to the wireless feedback from receiver about its location and power level (see Section 3.4).

3 SYSTEM DESIGN

In this section, we detail each component that contributes to the proposed system ChargeX.

3.1 Magnetic-beamforming in ChargeX

In this section, we derive the rules that govern magnetic beamforming in a MR-WPT system by involving an MTS between the Tx and Rx. The typical MR-WPT systems include two-coil and four-coil structures. The design of the four-coil system differs from the standard two-coil design in that it includes a drive coil and a load coil that are placed alongside the original transmitter and receiver coils. Previous research has confirmed that the four-coil structure is more efficient for in longer transmission distances [35], which makes it the preferred option for long-distance WPT in this work.

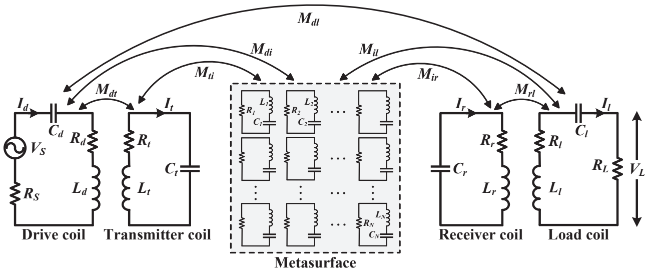

Figure 4: Simplified equivalent circuit model of MTS-assisted four-coil MR-WPT system. M_{dr}, M_{tr} and M_{tl} are still there but not shown in this figure.

The equivalent circuit model of the entire system is depicted in Figure 4. The MTS is located between the transmitter and receiver coils and consists of N units. Assuming that the drive coil is connected to an AC power source with a voltage V_S and a frequency f. Each unit cell of MTS can be represented as a resistance-inductor-capacitor (RLC) resonant circuit with the lumped circuit resistance R_i, inductance L_i and capacitance C_i, where $i = 1, 2, ..., N$. Moreover, the parameters of the four-coil structure are characterized by the self-inductance, capacitance, and resistance of each coil, as well as the mutual-inductance between certain pairs of coils. For example, R_d, L_d, and C_d represent the self-resistance, inductance, and capacitance of the drive coil, respectively. M_{ti} is the mutual-inductance between the transmitter coil and i^{th} MTS unit cell. Similarly, the current flowing through the drive coil, transmitter coil, receiver coil, load coil and each MTS unit cell are symbolized as I_d, I_t, I_r, I_l and I_i, respectively. R_L is the load resistor.

Building the relationship between PTE and capacitance C_i of MTS. According to the Kirchhoff voltage law (KVL) and the mutual coupling theories, the individual impedance of the resonant coils can be expressed as [18]:

$$\begin{cases} Z_d = R_d + j(\omega L_d - \frac{1}{\omega C_d}) \\ Z_t = R_t + j(\omega L_t - \frac{1}{\omega C_t}) \\ Z_i = R_i + j(\omega L_i - \frac{1}{\omega C_i}) \\ Z_r = R_r + j(\omega L_r - \frac{1}{\omega C_r}) \\ Z_l = R_l + j(\omega L_l - \frac{1}{\omega C_l}) \end{cases}, \tag{1}$$

where $\omega = 2\pi f$ in rad/s, and f is the resonant frequency elicited by $f = \frac{1}{2\pi\sqrt{LC}}$. The overall loop equation of the WPT system is as follows [18]:

$$\begin{bmatrix} V_S \\ 0 \\ 0 \\ \vdots \\ 0 \\ 0 \\ 0 \end{bmatrix} = \begin{bmatrix} Z_d + R_S & jwM_{dt} & jwM_{d1} & \cdots & jwM_{dN} & jwM_{dr} & jwM_{dl} \\ jwM_{dt} & Z_t & jwM_{t1} & \cdots & jwM_{tN} & jwM_{tr} & jwM_{tl} \\ jwM_{d1} & jwM_{t1} & Z_1 & \cdots & jwM_{1N} & jwM_{1r} & jwM_{1l} \\ \vdots & \vdots & \vdots & \ddots & \vdots & \vdots & \vdots \\ jwM_{dN} & jwM_{tN} & jwM_{1N} & \cdots & Z_N & jwM_{Nr} & jwM_{Nl} \\ jwM_{dr} & jwM_{tr} & jwM_{1r} & \cdots & jwM_{Nr} & Z_r & jwM_{rl} \\ jwM_{dl} & jwM_{tl} & jwM_{1l} & \cdots & jwM_{Nl} & jwM_{rl} & Z_l + R_L \end{bmatrix} \begin{bmatrix} I_d \\ I_t \\ I_1 \\ \vdots \\ I_N \\ I_r \\ I_l \end{bmatrix}. \tag{2}$$

Then according to the circuit theory, the voltage transfer function can be simplified as:

$$\frac{V_L}{V_S} = \frac{R_L I_l + M_{dl} I_d + M_{tl} I_t + \sum_{i=1}^{N} M_{il} I_i + M_{rl} I_r}{V_S}, \tag{3}$$

where V_L is the voltage across the load. The transmission scattering parameter S_{21}, is evaluated as:

$$S_{21} = (2V_L/V_S)\sqrt{R_S/R_L}, \tag{4}$$

and the PTE of the system can be calculated by:

$$\eta = |S_{21}|^2 \times 100\%. \tag{5}$$

To achieve impedance matching and maximum PTE, both the source resistance (R_S) and load resistance (R_L) are assumed to be 50Ω, so the PTE is directly related to the voltage transfer function $\frac{V_L}{V_S}$. Given the location and parameters of four coils, the mutual inductances M_{dl}, M_{tl} and M_{rl} are constant, while M_{il} is a variable due to the tunablility of MTS unit cells. According to the mutual coupling theory, the mutual inductance M_{il} depends on the permeability of the MTS units, which in turn depends on the capacitance of the diodes:

$$M_{il} = k^2 * \mu_0 * \mu_i * A_i / d_{il}, \tag{6}$$

where k is the wave vector in free space μ_0 is the permeability of free space A_i is the effective area of the i-th MTS unit cell d_{il} is the distance between the i-th MTS unit cell and the load coil. The relationship between the permeability of the i^{th} unit and its capacitance can be expressed as follows [18]:

$$\mu_i = \mu_0(1 + j\omega\tau_i)/(1 - j\omega\tau_i), \tag{7}$$

where μ_0 is the permeability of free space, τ_i is the time constant of the i^{th} varactor diode. The time constant of the varactor diode can be expressed as:

$$\tau_i = R_i C_i, \tag{8}$$

where C_i is the capacitance of the i^{th} unit, and R_i is the series resistance of the varactor diode.

Finally, we can build the relationship between the PTE η and the capacitance C_i of i^{th} MTS unit cell, by substituting Eq. 3, Eq. 4, Eq. 6, Eq. 7, Eq. 8 into Eq. 5. To maximize the PTE, we need to find the optimal combination of capacitances C_i that maximize the expression for η. This can be done by solving the following optimization problem:

$$\max_{C_i} \eta(C_1, C_2, ..., C_N) \tag{9}$$

subject to the constraints $C_{min} \leq C_i \leq C_{max}, \forall i = 1, 2, ..., N$, where C_{min} and C_{max} are the minimum and maximum values of the capacitance of each varactor diode.

The optimal combination of capacitances that maximizes PTE can be discovered by calculating PTE for various capacitance combinations, but this process can introduce significant time delay. To speed up scanning time, optimization problems can be solved using numerical methods like gradient descent or genetic algorithms, which are sensitive to initial values. In this work, we employ a simple yet effective coarse-to-fine scanning algorithm [6].

Beamsteering as receiver moves or rotates. Based on the aforementioned principle of metasurface-assisted magnetic-beamforming, the beam steers as the receiving coil moves or rotates, thereby allowing user change his/her device's location and orientation. This is because the mutual inductances M_{il} vary with the receiver's location and orientation, we can search for the ideal MTS configuration for the current location and orientation of the device. This process relies on real-time feedback from the receiver, which is elaborated in Section 3.4.2. Note that in static scenario, we can determine the optimal MTS configuration for maximum efficiency. While in mobile scenario, we apply course-to-fine grained scanning to find the suboptimal configuration. A full scan takes approximately 0.2 seconds, and efficiency decreases as movement speeds up.

Beamsteering to multiple receivers. The beam can also be steered to multiple directions. To simplify the capacitance control process of MTS, we divide the entire MTS to several subsurfaces that are responsible for steering the magnetic flux to each receiver, according to the coarse coarse-grained estimation of the location of multiple receivers (By sequentially setting one unit of the metasurface to work, the other units are all offset away from the operating frequency band). We can separately find the optimal configuration of each subsurface to maximize the PTE of each receiver. While it potentially reduces the power reaching each of the devices when beamsteering to multiple directions at the same time.

3.2 Transceiver coils and MTS design

Frequency selection. This work targets at wireless charging for small mobile devices. Considering the miniaturization of these devices, the receiver size needs to be small enough to be easily integrated into devices. Secondly, in order to ensure the potential of system's charging efficiency and distance, we select MR-WPT that requires larger transmitter and receiver coils. Despite introducing capacitance into the coils to adjust their resonant frequency, it is almost impossible to design small coils (i.e., less than 5 cm) at low frequencies (e.g., tens or hundreds of kHz). Therefore, to pursue spatial freedom and high efficiency, we opt for a higher frequency of

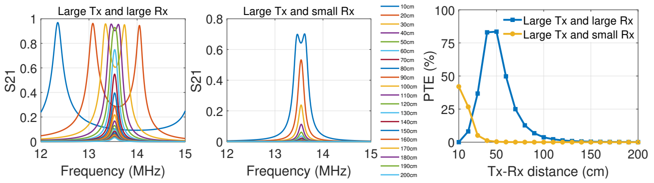

Figure 5: S21 and PTE results without MTS for varying Tx-Rx distances between 10cm to 200cm.

13.56 MHz (within the licensed frequency range of wireless charging) as the resonant frequency of the transceiver and the MTS in our design.

Transceiver coils design. After determining the resonant frequency, we design the charging coils in accordance with the design principles outlined in [5, 9]. Instead of adopting the symmetrical coil structure, we exploit a large-transmitter and small-receiver system considering the practical applications. We optimize the geometry parameters and capacitor values of charging coils to make them resonate at 13.56 MHz.

Simulation verification for transceiver coils. To verify the performance of transceiver coils, we simulate the WPT system consisting of the designed coils using the HFSS software. We consider the case where the Rx coil is much smaller than the Tx coil, as well as the case where the sizes of Tx and Rx coils are the same. The S21 and PTE results are shown in Figure 5, it can be seen that the designed transceiver coils resonate exactly at 13.56 MHz. We can also see that the PTE decreases as the Tx-Rx distance increases, especially when the size of the Rx coil is much smaller than that of the Tx coil. This demonstrates the necessity of involving an MTS to improve the PTE of WPT system.

MTS design. To change the magnetic flux to any direction by MTS, the MTS needs to be designed with both positive and negative permeability. As depicted in Figure 6, the higher the absolute value of the permeability of the MTS, the greater the deflection angle generated when the incident magnetic field passes through it. However, the problem is that as the absolute value of permeability increases, the imaginary part of the complex magnetic permeability increases, resulting in greater attenuation and thus reducing power transfer efficiency. To address this, we adopt a spiral-shaped resonator meta-atom structure that has been reported to show a higher quality-factor than the split ring resonator unit [16], and we optimize its parameters to make it resonant at 13.56 MHz. Finally, the MTS is composed of an array of meta-atoms with equal number of rows and columns. We utilize F4B material as the substrate of MTS.

Simulation verification for MTS. Figure 7 presents the simulation results of the permeability of the meta-atom. As shown in Figure 7(a), our optimized meta-atom structure has much lower loss compared to the traditional spiral meta-atom, which ensures low attenuation when adjusting over a wide range of angles. Figure 7(b) shows that the resonance frequency of the meta-atom can be changed by varying the capacitance integrated on the meta-atom, thereby changing the permeability at a given frequency. Figure 8 shows the magnetic field distribution of the WPT system with and without an MTS between the Tx and Rx. Obviously, the magnetic field at the Rx is very weak when there is no MTS, while with the MTS, the magnetic field is successfully focused to the Rx. In addition, compared with a uniform MTS, the uneven and adjustable MTS adopted in this paper provides greater improvement, regardless of the size of transceiver coils. Figure 9 demonstrates that MTS can steer the magnetic flux to multiple Rxs at different locations.

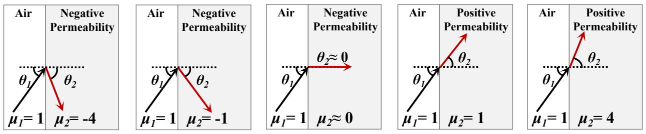

Figure 6: Magnetic boundary conditions of the MTS with various permeability, which hold $\tan\frac{\theta_1}{\theta_2} = \frac{\mu_1}{\mu_2}$.

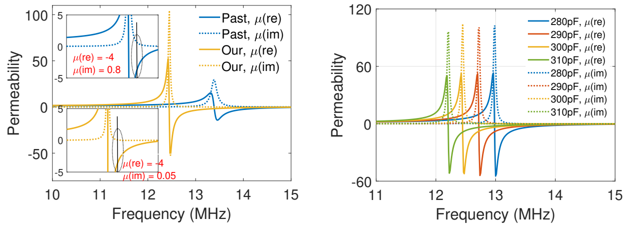

(a) Permeability comparison of different meta-atom structure.

(b) Varying permeability of our designed meta-atom.

Figure 7: Permeability results of MTS unit cell.

Lessons learned. To determine an optimal size of MTS, we simulated the MPT system with MTS composed of different number of meta-atom. The PTE increment $\Delta\eta$ caused by MTS is shown in Table 1. An interesting finding is that the PTE does not always increase with the MTS size. We found that the optimal MTS size (8×8 units, 48×48 cm^2) is not much larger than the Tx coil (i.e., 32 cm diameter). We guess this may be because the system focuses on near-field power transfer, when the MTS is too large, some outer units are not needed actually, but they still induce small loss. Anyway, this finding can guide people to determine the fabrication size of MTS according to the Tx size for a MR-WPT system.

3.3 MTS control system

Challenge: *How to achieve continuous and accurate capacitance control of each MTS unit cell?* To provide the required varying capacitances for each MTS unit cell, a multi-channel programmable power supply is necessary to offer varying

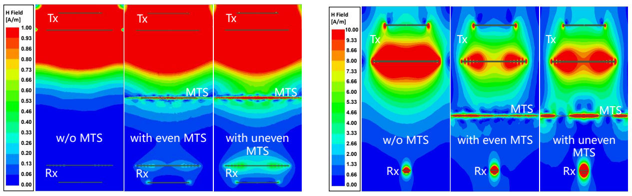

(a) Large Tx and large Rx.

(b) Large Tx and small Rx.

Figure 8: Magnetic field distribution of the WPT without MTS, with even MTS and with uneven MTS. Red color means stronger magnetic field.

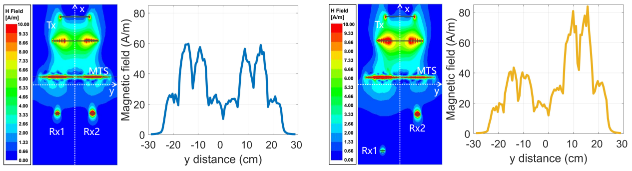

(a) Tx-Rx1 distance is same as Tx-Rx2 distance.

(b) Tx-Rx1 distance is larger than Tx-Rx2 distance.

Figure 9: Magnetic field steered to multiple receivers.

Table 1: Impact of MTS size on PTE increment $\Delta\eta$ (%). Case1: Tx/Rx diameter is $32/32$ cm, Tx-Rx distance is 60 cm; Case2: Tx/Rx diameter is $32/4$ cm, Tx-Rx distance is 30 cm.

MTS units	2 × 2	4 × 4	6 × 6	8 × 8	10 × 10	12 × 12
Case1	-23	9	34	36	29	26
Case2	-1	16	19	21	18	15

bias voltages to the integrated varactor diodes. Unfortunately, commercially available programmable power supplies have at most three channels, which is inadequate for our 64-channel requirements. On the other hand, using multiple switches to select capacitance may not achieve continuous control, thereby limiting the MTS's gain. Besides, due to the chip discretization and circuit errors, the actual capacitance may differ from the expected value. In this work, we designed a scalable DAC-based MTS control system, and proposed a software-based calibration to correct inherent diode errors. We provide more details here for others to follow.

Our control system uses ST's 7-series ARM7 chip as the primary control MCU and employs its 4-channel high-speed SPI interface with the corresponding I/O as the chip selection, to realize the control circuit for the 64-channel varactor diodes. The block diagram of control system is shown in Figure 10. To facilitate the future expansion of channels, the control system has been designed with a mother-daughter structure. The motherboard manages power, the main controller MCU, the communication interface, the programming interface, and the interface circuitry with the daughter board. On the other hand, the daughter board handles DAC, reference sources, impedance matching, signal amplification, variable capacitance circuits, and other related functions.

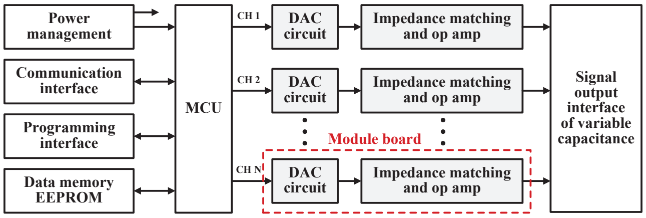

Figure 10: Block diagram of MTS control system.

This design offers a ***scalable and modular approach***, enabling the incorporation of additional daughter boards to increase the number of channels. The specific design of the key modules is as follows.

MCU and programming interface. We choose STM32F7 chip as the MCU, which can unleash the theoretical maximum performance of the Cortex-M7 core: at a CPU frequency of 216 MHz, performance tests have achieved a score of 1082 CoreMark / 462 DMIPS; It has rich peripheral interfaces, making it possible to implement various industrial control applications. As the main controller of the system, STM32F7 chip can meet the speed requirements for data refresh and the SPI communication interface required for the DAC. An external EEPROM data storage can be used to store user's configuration parameters, making it easy to store data and calibrate output parameters during later debugging.

Power management. The control system is powered by a wide input voltage DC-DC power supply. Upon entering the system, the power supply is divided into two channels separated by diodes. One channel is dedicated to powering the MCU (digital circuitry) via inputting a wide voltage to DC-DC converter to become 3.3 V. The other channel passes through a DC-DC module, generating positive voltage for the power supply of the analog component. The analog and digital power supplies are isolated by small resistors, which serve to prevent crosstalk of digital signals and improve the stability of the analog output.

Communication interface. To prevent interference from the host computer with the analog signal, we utilize an isolated communication interface to communicate with the host computer. The isolated portion of the power supply is powered by an isolated DC-DC module, while the digital part employs both a magnetic coupler and an optocoupler for data exchange. Additionally, our circuit includes a receiving collision suppression circuit, which enables the coexistence of RS485 and RS232 interfaces, making it easy to select a preferred communication interface later.

Module circuit interface. To support 64-channel control in this work, the main control board is equipped with 4 groups of module interface circuits, each featuring a standard SPI interface and 16 chip selection signals. This allows for easy control and writing of each signal on the module board.

Additionally, the socket is designed with a power supply, making it convenient to power the module part.

Module board circuit. In each module group, we designed a voltage reference circuit, a corresponding voltage follower circuit, and an amplifier circuit for the DAC. The digital signal written by the MCU into the DAC chip is converted into an analog signal relative to the reference voltage after passing through the DAC chip. Note that the commercial DAC module only supports voltage output up to 5 V, after impedance matching by a voltage follower, the analog signal enters an operational amplifier with a fixed gain, and is amplified to the voltage signal required by a varactor diode. The corresponding capacitance change is achieved through the change in voltage signal. Each group of output module consists of 16 identical DAC adjustment circuits, which provide 16 variable capacitance adjustments. The outputs are conveniently connected through an IDC socket for seamless board-level signal connection with the MTS. The switch speed of capacitance is around 10 μs.

To calibrate the capacitance error of the diodes, we incorporated a data memory into the control system, so that we can adjust the capacitance output based on the actual results obtained during testing. The calibrated ratio is stored in the data memory, and combined with the calibration coefficient during later use to achieve accurate capacitance output.

3.4 End-to-end wireless charging

In this section, we first answer how to deliver energy from a source device to the Tx coil, and how to extract energy from the Rx coil to the load device. Then we introduce the wireless communication scheme between the Tx and Rx.

3.4.1 Source and load circuits design. To enable wireless charging, the source circuit needs to match the operating frequency of the transceiver coils. We note that most of wireless charging systems work at lower frequency bands (i.e., tens or hundreds of KHz), To ensure both efficiency and compactness, we have opted a resonant frequency of 13.56 MHz for Tx and Rx coils. The exiting 13.56 MHz source circuits is designed for very low input power (1W), targeting low-power wearables [33]. In this work, we tailored the source circuit to support commonly desired power (i.e., 20W) for popular mobile phones at the higher 13.56 MHz frequency band. The source circuit is also designed with frequency adjustability to deal with the frequency shift of transceiver coils. Meanwhile, we customized the load circuit to establish communication with the source device and ensure proper connection to the receiver coil. The block diagrams of source and load circuits are shown in Figure 11.

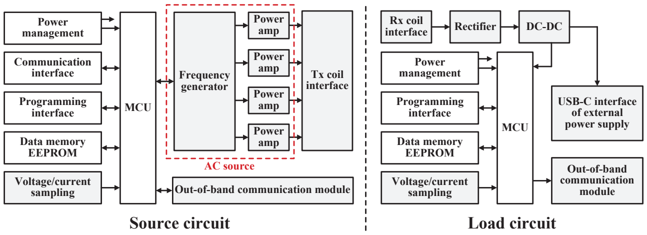

Figure 11: Block diagrams of source and load circuits.

Source circuit design. ***Challenge:*** *How to achieve required high power at such a higher frequency band?* In order to realize wireless charging at an adaptive desired frequency, We choose LTC6903 as the frequency generator since it is a low power self contained digital frequency source providing a precision frequency from 1 kHz to 68 MHz [23]. Since the conventional chip-level power amplifiers cannot meet the required power at this high frequency band, we propose employing multiple parallel high-frequency power amplifiers to achieve the desired power output. However, due to inherent hardware errors in the amplifiers and variations in wiring, it is challenging to ensure that each amplifier outputs the same power. Directly paralleling multiple amplifiers could lead to inaccurate power output and potentially damage the circuit board. To address this, we design corresponding matching capacitor for each amplifier and meticulously adjust the amplification factor of the peripheral circuit to achieve precise power output. A standard RC oscillator IC is used in conjunction with external matching capacitors and the main control MCU to achieve central frequency adjustment. The Tx uses a STM32F series MCU as the main control, which is designed with an on-board debugging interface and a data memory EEPROMA to store user's setting data. The main control MCU manipulates the output frequency of the frequency generator through the SPI interface. At the same time, a voltage and current sampling circuit is designed at the output end to realize real-time measurement of the output power. A low-dropout regulator (LDO) is also designed to provide stable and reliable working power supply for MCU.

Load circuit design. ***Challenge:*** *How to ensure high rectification efficiency?* We acknowledge that certain rectifier diodes are capable of operating at the designed frequency in this work, yet they support only a mA level current output. This is inadequate for mobile phone charging, which necessitates up to 2A of current. To ensure adequate current output, we employ multiple sets of high-frequency diodes in parallel to efficiently rectifies the high-frequency signal into a DC signal, and then stabilizes the power supply to 5 V through a DC-DC conversion circuit, so that can supply power to external user devices through a USBType-C interface. Since the Rx is expected to detect its charging state, a STM32F series MCU is utilized as the main control. Similar to the Tx, the LDO, on-board debugging interface and user data memory EEPROM are also designed at the Rx.

3.4.2 Wireless feedback. To ensure a seamless charging experience for users and minimize energy waste, the Tx requires real-time knowledge of the Rx's position and power level. Upon receiving a signal indicating that the Rx needs charging, the Tx switches to a discharge state by setting the frequency of the AC power source to the resonant frequency of the Tx coils. The MTS regulates the magnetic field in real-time, aligning it with the Rx to enable efficient charging. Once the Rx is fully charged, the Tx ceases the discharge process. For above purpose, the wireless charging system must be designed with communication capabilities.

Challenge: *How to obtain accurate feedback? There are several ways to get feedback such as coupling effect and out-of-band communication. However, those are susceptible to interference from obstacles and other electronic devices.* To deal with the interference issue, we propose to combine the coupling effect with out-of-band communication, this allows us to combine the voltage and current samples measured at both Tx and Rx to manipulate the MTS. We integrate the communication module into the source and load circuits. The real-time data communication between the Tx and the Rx is realized through the built-in UART interface of the main control MCU. Meanwhile, the working status of the communication module is controlled through the GPIO interface of the main control to achieve stable and reliable low-power communication. Finally, according to the power state feedback from receiver and discharge state of transmitter, the central controller can achieve real-time adjustment of the transmitting signal and MTS configuration.

Table 2: PTE increment $\Delta\eta$ (%) at different d_{tm} (cm). Tx/Rx diameter is 32/32 cm in this simulation, but the resulting law is similar to that of using small Rx (4 cm).

d_{tr} \ d_{tm}	5	10	20	30	40	50	60	70	80	90	100	110
80	16	38	38	36	34	34	36	38	-	-	-	-
100	12	24	24	23	22	21	22	22	23	24	-	-
120	9	17	17	16	15	15	15	15	15	16	17	17

3.4.3 Optimizing the deployment of MTS. In order to enhance PTE of the MTS-assisted wireless power transfer system, it is necessary to determine an optimal deployment of MTS. For the purpose, we conduct simulations under various distance between MTS and transceiver. The tunable MTS is located between the Tx and Rx. We denote the Tx-Rx, Tx-MTS and MTS-Rx distance as d_{tr}, d_{tm} and d_{mr}, respectively. We change the location of MTS from Tx end to Rx end by step of 10 cm. The simulation is repeated with three different Tx-Rx distance d_{tr} (i.e., 80 cm, 100 cm and 120 cm). Table 2 presents the PTE improvement under different deployments. We observe that $\Delta\eta$ of the system at shorter d_{tm} and at shorter d_{mr} are both high, due to the system symmetry. It is also explainable that MTS provides higher PTE improvement when MTS is closer to the transceiver since the magnetic field diffuses less before reaching the MTS in such case. Based on this observation, we prefer to place MTS close to Tx consider the mobility of Rx in practice. In this work, we integrate the MTS system into the Tx end to perform end-to-end wireless charging. Note that the MTS cannot be directly attached or too close to the transceiver (i.e., d_{tm} <10 cm), otherwise serious frequency shift will be caused due to coupling effect.

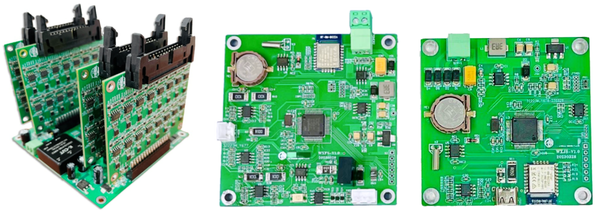

(a) MTS control board. (b) Source circuit. (c) Load circuit.

Figure 12: Hardwares designed for ChargeX.

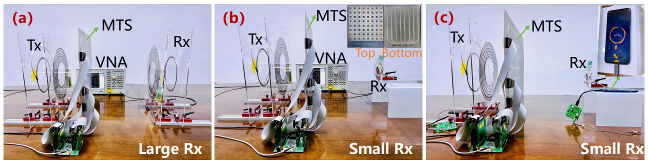

Figure 13: Default setup for PTE evaluation with VNA (a-b), and default charging setup with phone (c).

4 IMPLEMENTATION AND EVALUATION

4.1 Prototype implementation

We built a prototype of ChargeX using following components: the transceiver coils and an MTS including 8×8 inexpensive functional meta-atoms; the controller board, source and load circuits (see Figure 12); and a smartphone. The MTS is integrated into the Tx end and positioned 15 cm away from the Tx coil. The Rx coil and load circuit are small enough to be attached to the back of the phone. To charge the phone, the load circuit is connected to the USBType-C port, no modifications to the phone are needed.

We conducted experiments in a standard office room to evaluate ChargeX's performance. We measured PTE, charging time, and received power at different Tx-Rx distances and orientations. Note that we measured the Tx-Rx distance as the distance between the transmitter and receiver coils, not between the source and load coils.

4.2 PTE evaluation

We first test ChargeX's PTE by using vector network analyzer (VNA, Agilent E5062A), the default experimental setup is shown in Figure 13 (a-b).

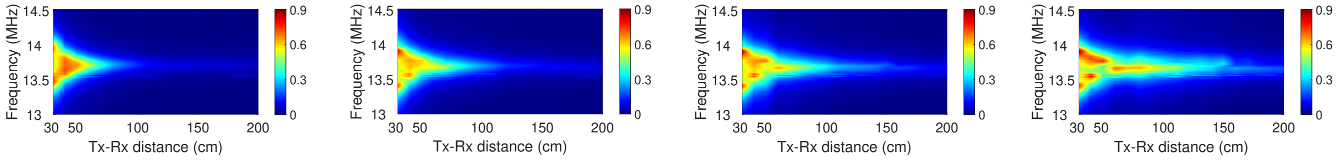

(a) Without MTS. (b) With MTS ($\mu = -4$). (c) With MTS ($\mu = -1$). (d) ChargeX.

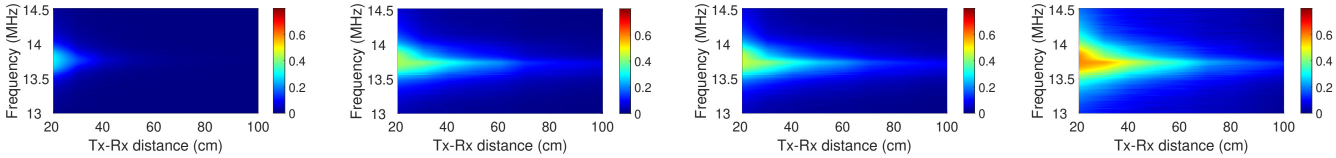

(e) Without MTS. (f) With MTS ($\mu = -4$). (g) With MTS ($\mu = -1$). (h) ChargeX.

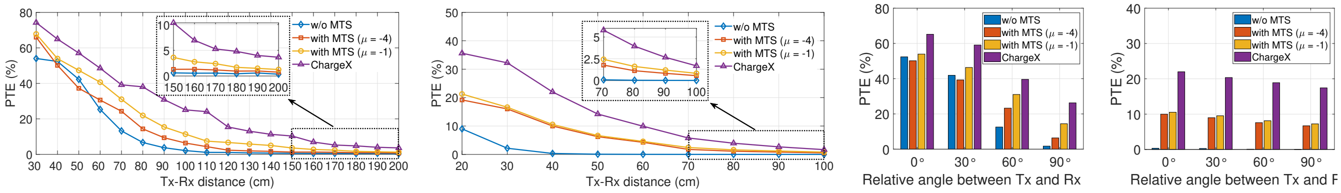

(i) Large Tx and large Rx. (j) Large Tx and small Rx. (k) Large Tx and large Rx. (l) Large Tx and small Rx.

Figure 14: S21 (a-h) and PTE (i-l) measurements under varying Tx-Rx distance/orientation. Red color in (a-h) indicates larger S21. (a-d, i, k), (e-h, j, l) are measured with large Tx and large Rx, large Tx and small Rx, respectively.

Comparison with other MTS-assisted WPT systems. Table 3 compares ChargeX with other reported MTS-based WPT systems. For fair comparison, the transfer distance between the Tx and Rx coils is normalized to the geometrical mean of Tx and Rx radius as $D_{norm} = D/\sqrt{r_T \cdot r_R}$ [30], where D, D_{norm}, r_T, and r_R represent the transfer distance, normalized distance, Tx radius, and Rx radius, respectively. We calculate the maximum transfer distance with PTE over 10% for comparison.

It can be seen that the WPT systems with an uneven MTS [8, 19] have shown overall improved PTE compared to the WPT systems with an even MTS [32, 37] given the same normalized transfer distance, while ChargeX is the first one that exhibits continuous tunability of MTS. This unique characteristic enables it to maximizly steer the outward magnetic flux toward the Rx, thus making it outperform other endeavors. In addition, ChargeX supports highest radius ratio between the Tx and Rx coils, which makes it more challenging to achieve effective beam alignment. Another significant difference between ChargeX and previous work is that ChargeX achieves end-to-end wireless charging.

Support for longer transfer distance. This experiment is designed to understand the PTE improvement brought by the MTS under varying Tx-Rx distance. To comprehensively verify the performance of MTS, We conduct experiment with both large and small Rxs.

Table 3: Comparison of ChargeX with other MTS-assisted WPT systems.

Ref.	Frequency (MHz)	Tx/Rx radius (mm)	Refraction index	Normalized distance	Continuous tunability
[37]	27	200/200	-1	3.5	No
[32]	5.57	20/20	-1	2.5	No
[8]	7.43	75/75	0, 1	6.2	No
[19]	6.78	300/75	$-1, -3$	7.8	No
ChargeX	13.56	160/160	$-4 \sim 0$	9.4	Yes
ChargeX	13.56	160/20	$-4 \sim 0$	10.6	Yes

Figure 14(a-h) shows the original S21 measurements obtained by the VNA, which is utilized to calculate the PTE plots as shown in Figure 14(i-j). It can be seen that the WPT systems with MTS show overall PTE improvement. Without the MTS, the PTE decreases significantly with the transfer distance. However, the decreasing slope of the PTE becomes slower when the MTS is inserted which means the MTS helps focus the magnetic flux, thereby increasing the PTE and transfer distance. To validate the performance of using continuously tunable MTS, we measure the PTE with MTS under four kinds of configuration: 1) All unit cells are tuned to $\mu = -1$; 2) All unit cells are tuned to $\mu = -4$; 3) The unit cells from outer to center are linearly tuned from $\mu = -4$ to $\mu = 0$. Obviously, the WPT system using the continuously tunable MTS shows the highest PTE, which demonstrate the necessarily of proposed ChargeX. The MTS with $\mu = -4$ shows the worst PTE since it suffers higher magnetic loss than the MTS with $\mu = -1$.

Resistance to orientation misalignment. This experiment is designed to answer how the Rx rotation affect ChargeX's

PTE. The Tx-Rx distance is set to 40 cm. We rotate Rx coil around the center point to four angles (0°, 30°, 60° and 90°) relative to Tx coil. At 0°, the Tx and Rx are ideally aligned; at 90°, the Tx and Rx are perpendicular to each other.

Figure 14(k-l) shows the PTE measurements of WPT system without and with MTS. From the figure, we can see that without an MTS, the PTE drops sharply as the deviation between the orientation of the Tx and Rx coils increases, especially when the Rx is perpendicular to Tx, almost no power can be transferred from Tx to Rx. In contrast, the negative impact of this orientation misalignment can be mitigated by using MTS, particularly through the use of ChargeX. Note that with the direction deviation between the Tx and Rx increases, the PTE corresponding to the small Rx coil decreases more slowly than the PTE of using large Rx coil. This is expected since when the Rx coil is too small, there can always be a relatively stable small amount of energy is transferred to the Rx coil.

4.3 Wireless charging evaluation

This section is designed to evaluate ChargeX's charging performance for various devices. The default experimental setup is shown in Figure 13(c).

Baselines. We compare ChargeX (built with large Tx and small Rx) with following systems: (a) three of the advanced commercial wireless chargers: MagSafe [24], Uhada [36] and WPC02ZM [25], their input power is the same as ChargeX (i.e., 20 W); (b) the advanced MR-WC prototype using magnetic beamforming [14]; (c) the prototype built with our designed transceiver coils, without involving MTS.

Full charging time at varying distance. To evaluate the charging speed of ChargeX as the Tx-Rx distance increases. We move the Rx to different locations, and measure the full charging time it takes the wireless charging system to charge the Honor V20 starting from a dead battery. We repeat the same experiments for ChargeX and the aforementioned baselines to compare their performance. However, since MagMIMO is not publicly available, we use its reported results for comparison. Figure 15 plots the full charging time for each system at varying Tx-Rx distance, which reveals the following information: 1) ChargeX's full charging time is shorter than the baselines at overall distance. 2) ChargeX can enable wireless charging up to 60 cm away, while the charging distance of commercial wireless chargers does not exceed 1 cm. In contrast, MagMIMO achieves the second longest distance (i.e., 40 cm), but it needs to be declared that ChargeX's overall size is much smaller than MagMIMO.

Received power at varying orientation. One may also wonder how ChargeX power transfer ability varies with the orientation of Rx. In our experiment, we rotate the Rx to make the relative angle between Tx and Rx change from 0° to 90° by step of 10°. At 0°, the Tx and Rx are ideally aligned; at 90°, the Tx and Rx are perpendicular to each other. In each run, we calculate the received power based on the voltage and current measurements at the Rx. Figure 16 shows that ChargeX is able to deliver the almost consistent power to Rx in all orientations even though the Rx coil is orthogonal to the Tx coil, which is similar to the behavior of MagMIMO [14]. This is possible because ChargeX can steer the magnetic flux based on the orientation of direction.

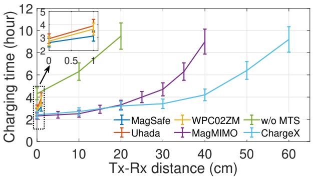

Figure 15: Varying charging distance.

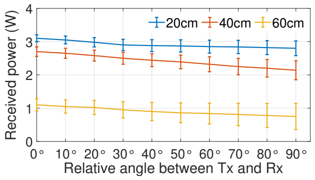

Figure 16: Varying Rx orientation.

Table 4: Charging the phone at real-word scenarios.

User quantity	Ave. time (h:mm)	Range (cm)	User status
1, 3	3:40, 5:50	20-30	Browsing the web
1, 2	4:05, 4:55	20-35	Playing games
1, 2	4:20, 5:15	20-40	Phone in pocket
1	5:45	10-60	Walking in place

Real-word case studies. We conduct experiments with multiple users to validate ChargeX's performance when users perform various activities with their phones. We also evaluate ChargeX with different smartphone models. Since ChargeX currently does not focus on the movement problem of multiple devices, in a multi-user cases, multiple phones engage in activities within a predetermined location, while the phone is allowed to move naturally with user in single-user case. In each experiment, the user was asked to attach the Rx coils and load circuit to his/her phone, hold the phone in hand or pocket, and naturally perform pre-designed daily activities within the charging range of Tx. During the experiment, the users check the battery level of their own phone every few minutes. The smartphones used in this experiment include: iPhone 12, Huawei Mate40 Pro, Xiaomi 10, Samsung Galaxy S7 edge, Honor V20, Nexus 6P and Pixel 2. All the phones are fully charged from a dead battery. The results in Table 4 indicate that ChargeX always can charge the user's phone independent of phone's model, and whether the user is browsing the web, playing games, walking in place, or put the phone in the pocket. From the results, we also acknowledge that the efficiency of charging diminishes with increased distance. Despite this limitation, it's noteworthy that ChargeX's effective charging range surpasses that of state-of-the-art prototype MagMIMO from its reported results [14].

Impact of charging on temperature. We measured the temperature changes during the process of charging the phone with our system ChargeX and three commercial wireless chargers, the temperature is measured by a infrared thermometer (DELIXI DM-5005). After up to ten hours of testing (two hours per test), the maximum temperature increase caused by our system ChargeX is below 1.5°, while the commercial chargers raise the temperature to an uncomfortable level. Specifically, Magsafe, Uhada, and WPC02ZM cause temperature increases of around 22°, 17°, and 24° respectively, which is more than 10× higher than ChargeX.

Safety validation. We also tested the touch voltage of the coils in ChargeX and found that it was always below 10 V, which is far below the safety threshold (50 V for adults, 25 V for children) [21]. This fully demonstrates that it is safe to touch the coils of ChargeX, even the coils are not isolated.

4.4 Microbenchmarks

In this section, we evaluate the effectiveness of the individual components that contribute to ChargeX.

Feedback scheme. To validate the effectiveness of feedback mechanism in ChargeX, we conduct a set of experiments without feedback, with past feedback scheme [14], and with ChargeX's feedback scheme. In each experiment, we move Rx away from Tx (Tx-Rx distance varies from 30 cm to 60 cm), and measure the snapshot of received power during moving process. The results shown in Figure 17 indicate that the proposed feedback scheme helps ChargeX better understand the status of Rx, and thus successfully steer the magnetic flux to Rx. The reason why ChargeX outperforms past feedback method is because it combines the voltage and current measurements from both transmitter and receiver, which is able to eliminate the interference issue during moving.

Frequency tunability. In order to verify the frequency tunability of the designed source circuit, we vary the resonant frequency of the Tx and Rx coils between 13 MHz and 14 MHz by changing the capacitance values of the coils, with a step size of ∼ 0.1 MHz. The default initial frequency of the source circuit was 13.56 MHz. We measured the PTE of the system with and without frequency control of the source circuit, and the results are shown in Figure 18. It can be seen that when there is frequency shift in the transceiver coils, our system can effectively adjust the input frequency to the resonant frequency of the coils, thus avoiding a sharp drop in PTE caused by frequency shift.

Increasing transmit power. Considering that the input power of some recent commercial wireless chargers is high as 50 − 70 W, we also redesign the source circuit to increase the input power of the system to 50 W. Experimental results show that the charging distance of ChargeX exceeds 1 **m** (see Figure 19). We believe that the distance can be further extended with the increase of input power, as well as enlarging the size of Tx coil.

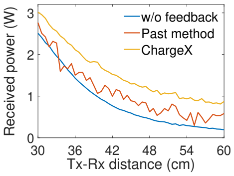

Figure 17: Feedback mechanism.

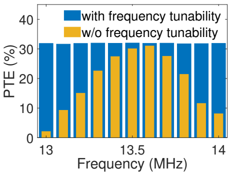

Figure 18: Frequency tunability.

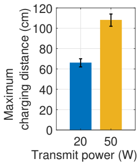

Figure 19: Increasing power.

5 RELATED WORK

ChargeX is broadly related to literature in following areas:

Traditional WPT systems. Traditional WPT systems use magnetic induction or magnetic resonance to transfer power wirelessly between a transmitter and a receiver [39]. In magnetic induction, the transmitter generates an oscillating magnetic field that induces a current in a nearby coil, which is then used to power a load [1, 12]. Magnetic resonance, on the other hand, uses resonant coils that are tuned to the same frequency to transfer power wirelessly. The resonant coils are coupled through a magnetic field, allowing for more efficient power transfer over longer distances [13, 27]. However, magnetic resonance technology's efficiency varies greatly depending on lateral and angular misalignments of Tx and Rx coils. To resolve these concerns, coil structures that can generate magnetic fields in all directions are required.

MIMO-based WPT systems. In recent years, many researchers pay attention to design the wireless charging antenna array using multiple coils for expanding spatial freedom [2, 34, 38]. MagMIMO is a magnetic beamforming system named that can charge a mobile phone at a distance of about 40 cm, regardless of the phone's orientation [14]. Camel is a context-aware MIMO MRC-WPT system, which enables adaptive charging of multiple devices simultaneously and achieve power transfer distance up to 50 cm [40]. In summary, MIMO-based WPT systems have many potential advantages over traditional single transceiver systems, including longer distance and higher reliability. However, these systems have increased complexity of implementation and deployment if they are expected to achieve transfer distance up to 1 m. In addition, they are sensitive to channel estimation errors. Ongoing research in this area is focused on developing new antenna designs.

MTS-assisted WPT systems. MTS-assisted WPT systems are a type of wireless power transfer technology that uses an MTS to control the direction and intensity of the magnetic field, which can enhance the coupling between the transmitter and receiver coils and reduce the energy loss during the power transfer process. Previous works showed that homogeneous MTS is efficient in improving symmetric WPT systems [32, 37]. However, homogeneous MTS has not been optimized for the asymmetric WPT system with a high radius ratio between the Tx and Rx coils [28]. The transfer efficiency of the asymmetric WPT system can be further increased by modifying the homogeneous to non-homogeneous MTS structures, aiming to confine the magnetic field into a small region, thus increasing the overall transfer efficiency [8, 19, 26]. Although promising, existing attempts focus more on simulation rather than the significant issues faced in building a real system. ChargeX aims to maximize the role of MTS in practical WPT systems, especially for asymmetric WPT system that has high radius ratio between Tx and Rx coils. Besides, we redesign the source/load circuits, and build a smart end-to-end wireless charging system that is demonstrated with phones.

6 LIMITATIONS AND CONCLUSION

ChargeX demonstrates the new possibilities for truly wireless charging in reality. However, our current prototype still faces few limitations that are left as future work:

Charging range: The charging distance of current ChargeX prototype is limited to ~ 1 m due to the compact receiver size and inherent limitation of near-field WPT. Given this charging range, we recommend deploying ChargeX in environments like buses or subways, where the movement of devices is relatively confined. Of course, the reported charging distance is not the maximum potential that ChargeX can achieve, partly because our current Tx coil and MTS are not large enough, at least compared to MagMIMO [14]. To cover a larger range, one could further increase the transmitter size and the transmit power within an acceptable range.

Charging multiple mobile devices: Although ChargeX is capable of charging multiple devices simultaneously, the current prototype does not pay attention to optimizing power allocation or tracking the movements of these devices. Significant challenges emerge in offering real-time feedback and efficient energy distribution when multiple devices are in motion. Future work could draw insights from context sensing [40] for smart charging of multiple mobile devices.

Despite these limitations, ChargeX marks an important step towards enabling long-range, flexible and safe wireless charging. The achievement of the above goals are attributed to a series of new hardware designs and feedback mechanism. Aside from its benefits for small mobile devices, the design of ChargeX could also be extended to wireless charging systems for electric vehicles while they are in motion. More importantly, ChargeX drives new directions in wireless research that introduce the smart MTS to extend the power transfer range in near/far field. It also motivates new source and load circuit designs that enable both power transfer and robust wireless communication between transmitter and receiver at desired frequency bands.

ACKNOWLEDGEMENT

This research was supported in part by the National Natural Science Foundation of China under Grant No. 62202256, 62122095, 62341201, 62072472 and 62302260, the China Postdoctoral Science Foundation No. 2023M731956, and a grant from the Guoqiang Institute, Tsinghua University.

REFERENCES

[1] Dukju Ahn and Songcheol Hong. 2012. A study on magnetic field repeater in wireless power transfer. *IEEE Transactions on Industrial Electronics* 60, 1 (2012), 360–371.

[2] Seong-Hyeop Ahn, Na-Rae Kwon, Min-Seong Kim, and Wang-Sang Lee. 2022. Design and Implementation of Wireless Charging Antenna Array Using Highly Isolated Coils for Expanding Spatial Freedom. In *2022 Wireless Power Week (WPW)*. IEEE, 39–43.

[3] Esraa Mousa Ali, Mohammad Alibakhshikenari, Bal S Virdee, Mohammad Soruri, and Ernesto Limiti. 2021. Efficient wireless power transfer via magnetic resonance coupling using automated impedance matching circuit. *Electronics* 10, 22 (2021), 2779.

[4] Mohammed H Alsharif, Abu Jahid, Anabi Hilary Kelechi, and Raju Kannadasan. 2023. Green IoT: A review and future research directions. *Symmetry* 15, 3 (2023), 757.

[5] Yuan Cao, Zhigang Dang, Jaber A Abu Qahouq, and Evan Phillips. 2016. Dynamic efficiency tracking controller for reconfigurable four-coil wireless power transfer system. In *2016 IEEE Applied Power Electronics Conference and Exposition (APEC)*. IEEE, 3684–3689.

[6] Lili Chen, Wenjun Hu, Kyle Jamieson, Xiaojiang Chen, Dingyi Fang, and Jeremy Gummeson. 2021. Pushing the Physical Limits of IoT Devices with Programmable Metasurfaces. In *18th USENIX Symposium on Networked Systems Design and Implementation (NSDI 21)*. 425–438.

[7] Kun Woo Cho, Mohammad H Mazaheri, Jeremy Gummeson, Omid Abari, and Kyle Jamieson. 2023. {mmWall}: A Steerable, Transflective Metamaterial Surface for {NextG}{mmWave} Networks. In *20th USENIX Symposium on Networked Systems Design and Implementation (NSDI 23)*. 1647–1665.

[8] Yeonje Cho, Seongsoo Lee, Dong-Hyun Kim, Hongseok Kim, Chiuk Song, Sunkyu Kong, Junyong Park, Chulhun Seo, and Joungho Kim. 2017. Thin hybrid metamaterial slab with negative and zero permeability for high efficiency and low electromagnetic field in wireless power transfer systems. *IEEE Transactions on Electromagnetic Compatibility* 60, 4 (2017), 1001–1009.

[9] Dean Clark. 2018. Considerations When Designing a Wireless Charging System. *Abracon, Spicewood* (2018).

[10] DC Power Supply 2023. DC Power Supply. Website.

[11] Xiaoran Fan, Longfei Shangguan, Richard Howard, Yanyong Zhang, Yao Peng, Jie Xiong, Yunfei Ma, and Xiang-Yang Li. 2020. Towards flexible wireless charging for medical implants using distributed antenna system. In *Proceedings of the 26th annual international conference on mobile computing and networking*. 1–15.

[12] Siu Lau Ho, Junhua Wang, WN Fu, and Mingui Sun. 2011. A comparative study between novel witricity and traditional inductive magnetic coupling in wireless charging. *IEEE Transactions on Magnetics* 47, 5 (2011), 1522–1525.

[13] SY Ron Hui. 2016. Magnetic resonance for wireless power transfer. (2016).

[14] Jouya Jadidian and Dina Katabi. 2014. Magnetic MIMO: How to charge your phone in your pocket. In *Proceedings of the 20th annual international conference on Mobile computing and networking*. 495–506.

[15] Morris Kesler et al. 2013. Highly resonant wireless power transfer: safe, efficient, and over distance. *Witricity corporation* (2013), 1–32.

[16] T Kipp, H Welsch, Ch Strelow, Ch Heyn, and D Heitmann. 2006. Optical modes in semiconductor microtube ring resonators. *Physical review letters* 96, 7 (2006), 077403.

[17] Andre Kurs, Aristeidis Karalis, Robert Moffatt, John D Joannopoulos, Peter Fisher, and Marin Soljacic. 2007. Wireless power transfer via strongly coupled magnetic resonances. *science* 317, 5834 (2007), 83–86.

[18] Hans-Dieter Lang and Costas D Sarris. 2017. Optimization of wireless power transfer systems enhanced by passive elements and metasurfaces. *IEEE Transactions on Antennas and Propagation* 65, 10 (2017), 5462–5474.

[19] Woosol Lee and Yong-Kyu Yoon. 2020. Tunable metamaterial slab for efficiency improvement in misaligned wireless power transfer. *IEEE Microwave and Wireless Components Letters* 30, 9 (2020), 912–915.

[20] Jiachun Li, Yan Meng, Le Zhang, Guoxing Chen, Yuan Tian, Haojin Zhu, and Xuemin (Sherman) Shen. 2023. MagFingerprint: A Magnetic Based Device Fingerprinting in Wireless Charging. In *IEEE Conference on Computer Communications (INFOCOM)*. IEEE, 1–10.

[21] Limit values 2023. Limit values. Website.

[22] Qingwen Liu, Mingliang Xiong, Mingqing Liu, Qingwei Jiang, Wen Fang, and Yunfeng Bai. 2022. Charging a smartphone over the air: The resonant beam charging method. *IEEE Internet of Things Journal* 9, 15 (2022), 13876–13885.

[23] LTC6903 2023. LTC6903. Website.

[24] MagSafe Charger 2023. MagSafe Charger. Website.

[25] Mi 20W Wireless Charging Stand 2023. Mi 20W Wireless Charging Stand. Website.

[26] Thanh Son Pham, Bui Xuan Khuyen, Bui Son Tung, Thu Trang Hoang, Van Dai Pham, Quang Minh Ngo, and Vu Dinh Lam. 2021. Enhanced efficiency of asymmetric wireless power transmission using defects in 2D magnetic metamaterials. *Journal of Electronic Materials* 50 (2021), 443–449.

[27] Thanh Son Pham, Thao Duy Nguyen, Bui Son Tung, Bui Xuan Khuyen, Thu Trang Hoang, Quang Minh Ngo, Le Thi Hong Hiep, and Vu Dinh Lam. 2021. Optimal frequency for magnetic resonant wireless power transfer in conducting medium. *Scientific Reports* 11, 1 (2021), 18690.

[28] Thanh Son Pham, Aruna Kumara Ranaweera, Duc Viet Ngo, and Jong-Wook Lee. 2017. Analysis and experiments on Fano interference using a 2D metamaterial cavity for field localized wireless power transfer. *Journal of Physics D: Applied Physics* 50, 30 (2017), 305102.

[29] Bilal Sanauddin Pirzada, Kinza Shafique, Syed Arsalan Jawed, Irfan Muqim, Syed Usman Amin, Faiqa Abubaker, Fahd Khan, Muhammad Aaquib Shahbaz, Muhammad Junaid Jabbar, and Mustafa Fazal Abbas. 2023. A mid-range wireless power transfer system for portable electronic devices using beam forming. *Analog Integrated Circuits and Signal Processing* (2023), 1–15.

[30] Anil Kumar RamRakhyani, Shahriar Mirabbasi, and Mu Chiao. 2010. Design and optimization of resonance-based efficient wireless power delivery systems for biomedical implants. *IEEE transactions on biomedical circuits and systems* 5, 1 (2010), 48–63.

[31] Resonant inductive coupling 2023. Resonant inductive coupling. Website.

[32] Erik Saturnino Gámez Rodríguez, Anil Kumar RamRakhyani, David Schurig, and Gianluca Lazzi. 2016. Compact low-frequency metamaterial design for wireless power transfer efficiency enhancement. *IEEE Transactions on Microwave Theory and Techniques* 64, 5 (2016), 1644–1654.

[33] ROHM Wireless Charging Coil Transmitter 2023. ROHM Wireless Charging Coil Transmitter. Website.

[34] Hongru Sun, Hai Lin, Fengchao Zhu, and Feifei Gao. 2017. Magnetic resonant beamforming for secured wireless power transfer. *IEEE Signal Processing Letters* 24, 8 (2017), 1173–1177.

[35] Yixuan Sun and Stephen Beeby. 2021. Simulation of 2-Coil and 4-Coil Magnetic Resonance Wearable WPT Systems. In *Proceedings*, Vol. 60. MDPI, 13.

[36] Uhada Charger 2023. Uhada Charger. Website.

[37] Bingnan Wang, Koon Hoo Teo, Tamotsu Nishino, William Yerazunis, John Barnwell, and Jinyun Zhang. 2011. Experiments on wireless power transfer with metamaterials. *Applied Physics Letters* 98, 25 (2011), 254101.

[38] Gang Yang, Mohammad R Vedady Moghadam, and Rui Zhang. 2016. Magnetic beamforming for wireless power transfer. In *2016 IEEE International Conference on Acoustics, Speech and Signal Processing (ICASSP)*. IEEE, 3936–3940.

[39] Zhen Zhang, Hongliang Pang, Apostolos Georgiadis, and Carlo Cecati. 2018. Wireless power transfer—An overview. *IEEE Transactions on Industrial Electronics* 66, 2 (2018), 1044–1058.

[40] Hao Zhou, Zhao Chen, Wangqiu Zhou, Haisheng Tan, Panlong Yang, and Xiang-Yang Li. 2021. Camel: Context-aware magnetic mimo wireless power transfer with in-band communication. In *IEEE Conference on Computer Communications (INFOCOM)*. IEEE, 1–10.

[41] Jiafeng Zhou, Pei Zhang, Jiaqi Han, Long Li, and Yi Huang. 2021. Metamaterials and metasurfaces for wireless power transfer and energy harvesting. *Proc. IEEE* 110, 1 (2021), 31–55.

A STRUCTURES OF TRANSCEIVER COILS AND MTS

In this work, we utilize a system with large Tx coil and small Rx coil, based on the practical consideration that the Rx coil can be seamlessly integrated into small mobile devices. The geometric parameters of coils are shown in Figure 20 (a).

For MTS, we adopt a spiral-shaped resonator meta-atom structure and optimize its parameters to make it resonant at the desired frequency band. The structural schematic and geometric parameters of the MTS are depicted in Figure 20 (b).

B SCHEMATIC OF DAC CIRCUIT

Figure 21 illustrates the circuit schematic of the DAC module board, comprising a voltage reference circuit, a voltage follower circuit, and an amplifier.

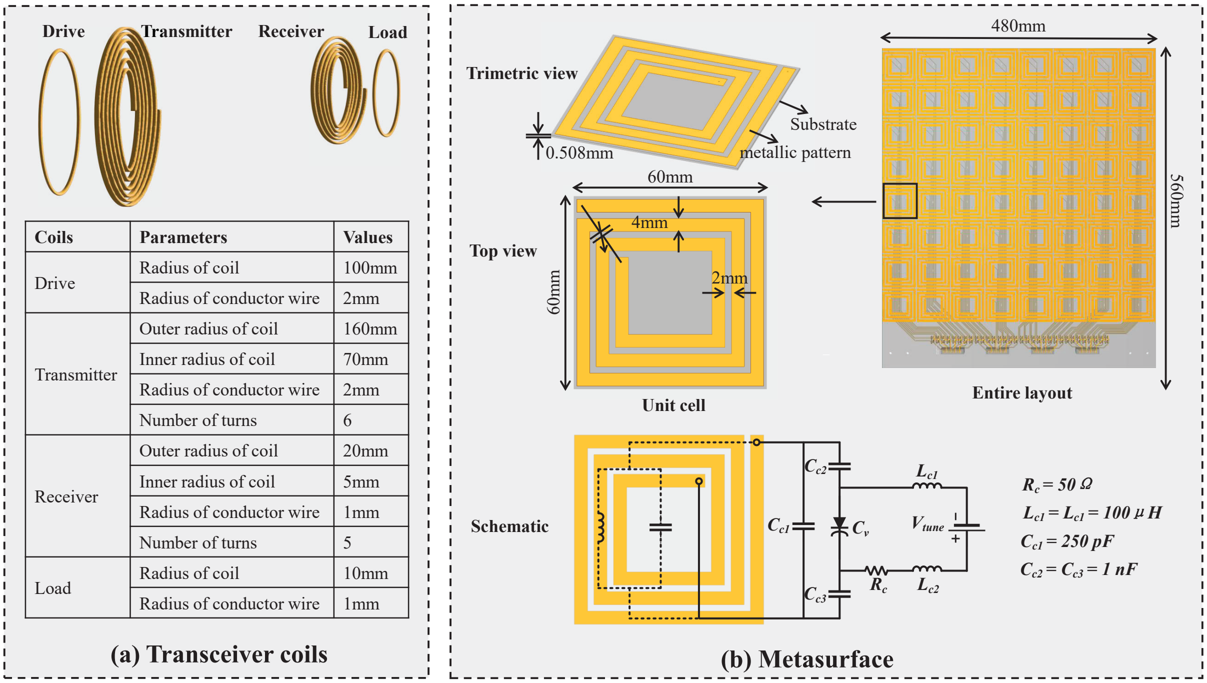

Coils	Parameters	Values
Drive	Radius of coil	100mm
	Radius of conductor wire	2mm
Transmitter	Outer radius of coil	160mm
	Inner radius of coil	70mm
	Radius of conductor wire	2mm
	Number of turns	6
Receiver	Outer radius of coil	20mm
	Inner radius of coil	5mm
	Radius of conductor wire	1mm
	Number of turns	5
Load	Radius of coil	10mm
	Radius of conductor wire	1mm

Figure 20: Structural schematic and geometric parameters of transceiver coils and MTS.

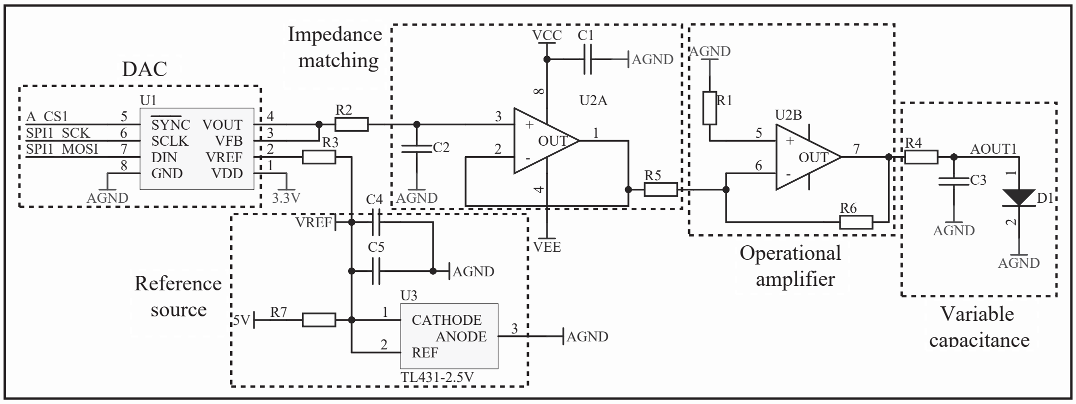

Figure 21: Circuit schematic of the DAC module board.